CORROSION RESISTANCE EVALUATION OF THE DIFFERENT ZONES ON THE AA2024-T3 AND AA7475-T651 ALLOYS WELDED BY FSW

C.P. Abreu[a,c], H.G. de Melo[b], N. Pébère[d], N.V.V. Mogili[e], I. Costa[c], V. Vivier[a]

[a]*LISE-CNRS-UMR 8235, Université Pierre et Marie Curie, Paris, France*
[b]*Universidade de São Paulo, Depto de Engenharia Metalúrgica e de Materiais, São Paulo, Brasil*
[c]*Instituto de Pesquisas Energéticas e Nucleares, IPEN/CNEN-SP, São Paulo, Brasil*
[d] *Université de Toulouse, CIRIMAT, UPS/INPT/CNRS, France*
[e]*Centro Nacional de Pesquisa em Energia e Materiais (CNPEM), Laboratório Nacional de Nanotecnologia(LNNano), Campinas - SP, Brasil*

The aeronautic industry has a great interest in joining dissimilar aluminium alloys used in different parts of an aircraft. The Friction Stir Welding (FSW) process has been considered an effective alternative to conventional techniques for the welding of high strength aluminium alloys. However, this procedure results in zones with different microstructures due to thermal and thermomechanical effects involved during the joining process, leading to the formation of the thermomechanically affected zone (TMAZ), the heat affected zone (HAZ), the stir zone (nugget), and the unaffected base metal (BM). As the corrosion resistance of materials depends on their microstructures, the aim of this study was to investigate the intrinsic corrosion resistance of the different zones of the AA2024-T3 and AA7475-T761 alloys welded by FSW, without considering the coupling effects between the different zones. This was achieved by evaluating the corrosion resistance of each individual zone in 0.1 M Na_2SO_4 + 1 mM NaCl solution by electrochemical techniques, such as open circuit potential measurements, polarization curves, and electrochemical impedance spectroscopy, using an electrochemical cell with an exposed area of 0.78 mm^2. The electrochemical results showed that the lowest corrosion resistance was associated to the nugget zone, on which a galvanic coupling between the 2024 and 7475 alloys takes place. The corrosion resistance was also lowered on the TMAZ of both alloys. This behaviour was associated to the enhanced precipitation of the η phase ($MgZn_2$) at the grain boundaries in the 7475 alloy and to the coarsening of S phase (AlCuMg) precipitates in the 2024 alloy, both processes favoured by the thermomechanical effects in these specific zones as demonstrated by TEM analysis.

Keywords: FSW, aluminium alloys, localized corrosion, microstructure, EIS.

Introduction

Weight reduction and durability of the parts used in aircraft are of prime importance for the aeronautical industry, allowing a longer life, reducing the number of repairs and fuel consumption, besides reducing the amount of harmful gases emissions to the atmosphere[1]. This can be achieved whether by reducing the density of the materials (*e.g.* by replacing heavy materials with lighter aluminium alloys) or by using new joining techniques in order to replace rivets and the overlapping of plates.

Fusion-based welding techniques are not effective for high strength aluminium alloys, such as those of the 2xxx and 7xxx series. For these materials, the difference between the thermal expansion coefficients of the solidified regions and the film of the liquid phase results in cracks in the final solidification stage of the weld bead, thus seriously damaging the mechanical properties of the joint[4].

The Welding Institute (TWI) developed in 1990 and patented in 1991 a linear friction welding procedure, designated Friction Stir Welding (FSW), for which no fusion of the welding bead takes place, *i.e.*, it is a solid-state process. This method results in a lower distortion, improved mechanical and metallurgical properties and reduced residual stresses. In this process, the pin of a non-consumable rotating tool traverses the materials to be welded up to the tool shoulder under appropriate conditions[5]. The friction of the pin and tool shoulder at the welding joint promotes heat and plastic deformation of the materials creating a plasticized zone which are joined by an applied forging pressure.

Four zones with different microstructures are generated in the FSW process, namely the zone of mixture (ZM) or nugget, the thermomechanically affected zone (TMAZ), the heat affected zone (HAZ) beside the unaffected areas of the base metal (BM). As there is a recognized correlation between microstructure and corrosion resistance of a material, these zone can exhibit different corrosion behaviour, which can give rise to galvanic coupling, particularly at the welding between dissimilar alloys.

The alloys of the 2xxx and 7xxx series are precipitation hardened and can be thermally treated[2,3]. In these materials, intermetallic particles, such as Al-Cu-(Mg), Al-Cu-Fe-(Mn) and $MgZn_2$ can be formed during the solidification process and their different electrochemical behaviour from that of the matrix favours the development of localized corrosion[3]. Besides these micrometric particles, nanometric dispersed particles and hardening precipitates formed during natural or artificial aging are also found in these alloys.

Regarding the nanometric particles in the 2024 alloy microstructure, the following phases are usually found: $Al_{20}Cu_2Mn_3$ dispersoids, which are rod-shaped particles of about 200 nm; S-phase intragranular precipitates (Al_2CuMg) needle-like shaped ranging from 8 to 30 nm, and platelet GPB zones with dimensions of approximately 0.2 nm, which are very difficult to visualize, even by transmission electron microscopy. Besides, intergranular rod-shaped S phase precipitates, with dimensions between 100 and 400 nm, can also be formed under particular conditions[3-7]. In relation to the nanometric-size compounds present in the 7475 alloy, Aval (2015) found the following phases: Al_3Zr spherical particles of about 50 nm; intragranular η '/ η particles (*i.e.* $MgZn_2$) of 5 to 75 nm (also reported by Li (2009) as rod-shaped precipitates), as well as GPB-like zones as platelets, with dimensions from 5 to 20 nm.

Some researchers have investigated the mechanical properties and the evolution of the different microstructural zones formed during FSW of similar alloys[6]. Moreover, Sidane[8] *et al.* (2015) and Donatus[9] *et al.* (2015) have demonstrated the relationship between FSW parameters, microstructure, hardness, and the electrochemical behaviour of dissimilar aluminium

alloys joined by FSW. Most of the studies on the corrosion resistance of friction stir welded (FSWed) alloys have investigated the effect of galvanic coupling of adjacent areas with different microstructures, whereas the corrosion behaviour of the different zones was not individually investigated. The aim of this study was to characterize separately the corrosion resistance of each welded zones resulting from FSW in association with their microstructure.

Materials and methods

Materials

The materials investigated in this study were 2.0 mm thick sheets of the AA2024-T3 and AA7475-T761 alloys joined by FSW (in the assembly, the 2024 sheet was positioned at the advancing side). The chemical compositions of both alloys are shown in Table 1.

Table 1. Chemical compositions (wt. %) of the tested aluminium alloys.

Element	Al	Mg	Cu	Zn	Si	P	S	Ca	Ti	Cr	Mn	Fe
2024	92.3	1.60	4.80	0.08	0.19	0.03	0.02	0.04	0.05	0.04	0.64	0.22
7475	89.4	1.90	1.70	6.20	0.15	0.03	0.05	0.06	0.04	0.22	0.02	0.12

Methods

Microstructural characterization of the FSWed alloys was performed by optical microscopy - OM (Leica DM LM) and by scanning electron microscopy - SEM (FEI Quanta 600). Samples were ground with sandpaper (#600, #800, #1200, #4000), polished with alumina down to 1 μm, thoroughly washed with ethanol, acetone and then dried in a hot-air stream. For OM analysis, the samples were further etched in Keller's reagent (10 mL HF + 15 mL HCl + 25 mL HNO_3 + 50 mL deionized water) at room temperature during 30 s and successively washed in deionized water, ethanol and dried under a hot air stream prior to observations.

The transmission electron microscopy (TEM) images were obtained using a JEOL 2100 and a FEI Titan cubed Themis (double corrected) operating at 200 kV and 300 kV, respectively. 3 mm disk shaped specimens were cut out of each weld zone, which were then thinned using a standard approach involving mechanical and dimple grinding and finally ion milling using Precision Ion Polishing System (PIPS). The compositions of the intragranular and intergranular precipitates were determined in Scanning TEM (STEM) mode using either Oxford X-Max^N windowless EDX detector in Jeol 2100 microscope or Titan's four windowless silicon drift detector system.

The DSC measurements were performed with a Mettler-Toledo 822 apparatus, under 99.999% purity nitrogen atmosphere, in the temperature range between 50 °C and 550 °C, at a heating rate of 10 °C / min. Samples were cut from each zone formed after welding by FSW, in squares with dimensions of 4 mm x 4 mm and 2 mm thick. The samples were placed in high purity aluminium crucibles of 5 mm in diameter. During the experiment the sample in crucible and an empty crucible (used as reference) were placed on a metal disk, the differential heat flow being controlled by thermocouples, thus allowing the DSC curves of each sample, presented as heat flux as a function of temperature or time, to be obtained.

For the electrochemical measurements, a three-electrode cell was used with an Ag/AgCl (3M KCl) reference electrode and a platinum sheet as counter electrode. The exposed area of the

working electrode was 0.78 mm^2. The electrolyte was a 0.1 M Na_2SO_4 and 1mM NaCl solution. Electrochemical measurements were performed on the unaffected areas of the two aluminium alloys (BM) and on all zones affected by the FSW process (TMAZ, HAZ and nugget).

Electrochemical impedance spectroscopy (EIS) experiments were carried out at the open circuit potential (OCP) using a Solartron 1287 potentiostat and a Solartron 1250 frequency response analyser. The applied potential sine-wave perturbation was 10 mV_{rms}. The EIS diagrams were obtained from 63 kHz to 10 mHz with 9 points per frequency decade. The diagrams were acquired after one hour of stabilization of the OCP, which was also recorded.

Anodic polarization curves were obtained using the same electrochemical cell employed in the EIS tests after 1.5 h immersion in the electrolyte. The anodic scans were started 30 mV below the OCP and were carried out at a scan rate of 0.500 mV s^{-1}. All electrochemical experiments were carried out in triplicate to evaluate reproducibility.

Results

Surface and microstructure characterization of the aluminium alloys welded by FSW

The macrograph presented in Figure 1 show the delimitation over the different weld zones and the optical micrographs for FSWed 2024-T3 and 7475-T651 alloys.

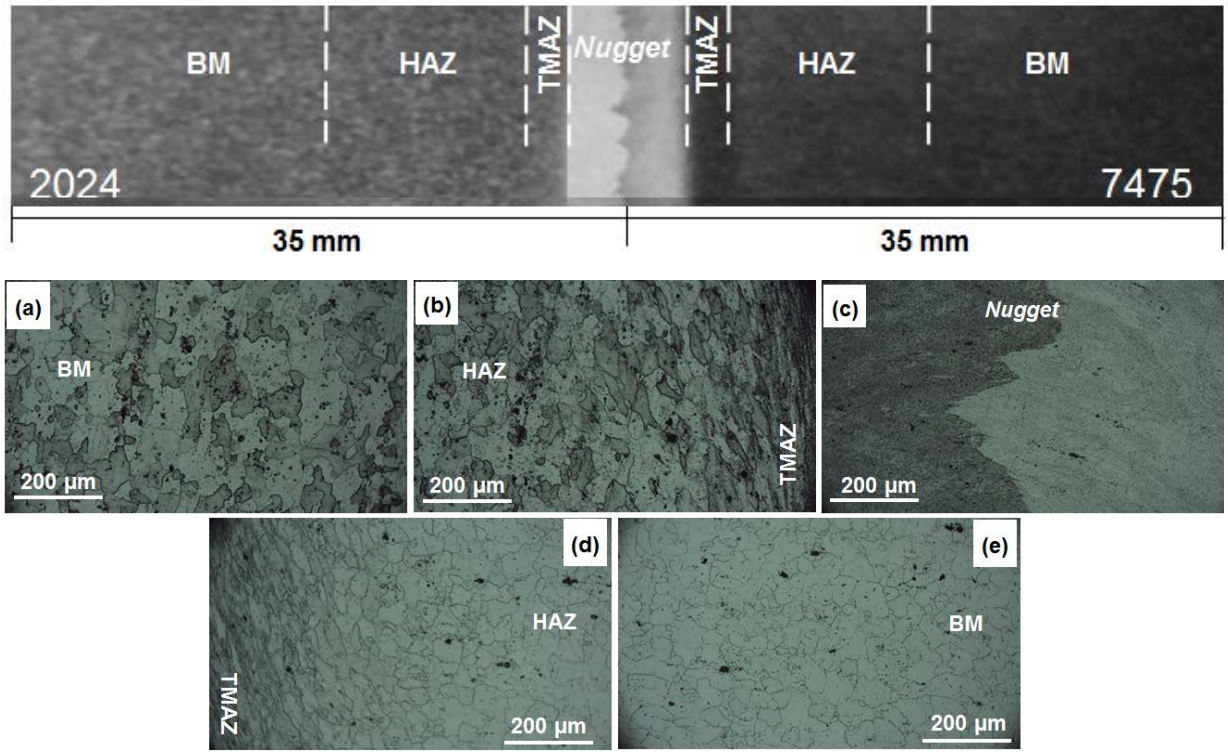

Figure 1: Macrographs of the welded joint and optical micrographs (a-e) of the different zones formed in FSWed 2024-T3 and 7475-T651 alloys. Images acquired after Keller's reagent etching.

The small grains of both alloys cannot be clearly identified in the nugget zone because of their tiny sizes as a result of the dynamic recrystallization process in this zone (Figure 1(c)). The grains of the HAZ and of the BM of the two alloys (2024 and 7475) are very similar (Figure 1(a) and (e)). The thermomechanical deformation at the TMAZ of the two alloys (Figure 1(b) and (d)), in turn, resulted in highly deformed grains in the direction of the tool rotation. This deformation is imposed by the friction and shear stress of the tool shoulder

against the metal surface and by the high temperatures reached during the process, allowing plastic deformation.

Figure 2 shows the TEM micrographs of the BM and the TMAZ zones of the 2024 alloy side of FSWed joint.

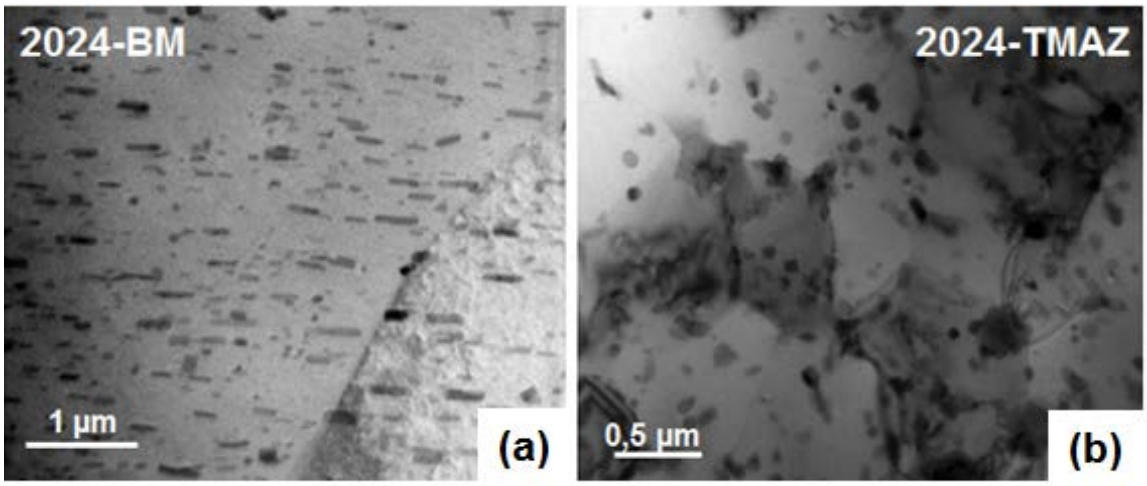

Figure 2: TEM micrographs of the unaffected zone (BM) (a) and the thermomechanically affected zone (TMAZ) (b) of the 2024-T3 alloy side of the FSWed joint.

The microstructure of the 2024 BM shows a large amount of rod-shaped dispersoids within the grains, Figure 2(a), in addition to few irregular precipitates. Chemical analysis by EDS of these microstructural features have shown that they present different compositions as shown in Figure 3. The rod-shaped precipitates are rich in Cu and Mn (Al-Cu-Mn), and their dimensions are about 200 nm, which is within the range determined in the work of Guillaumin *et al* (1999). In addition, a fine S-phase precipitate (Al_2CuMg) was also found at grain boundaries, possibly formed during natural aging of the alloy. The dispersoids were mainly distributed inside the grains and very few were located at the grain boundaries.

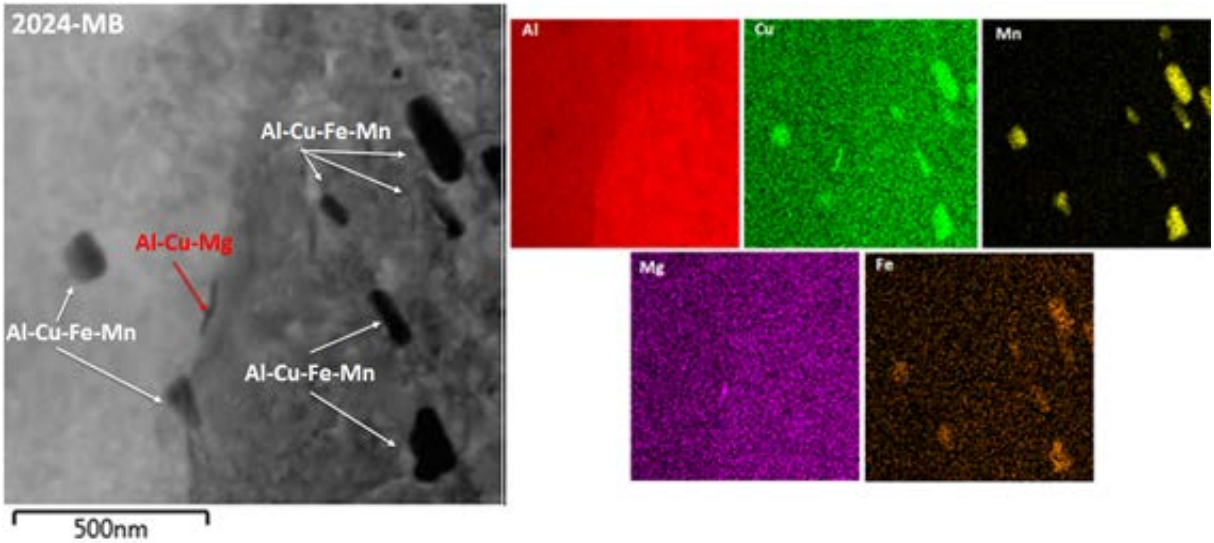

Figure 3: Micrographs obtained by Bright Field-STEM of precipitates in the BM of the 2024 alloy and EDS mapping of the regions.

The TMAZ of the 2024 alloy (Figure 4) shows a microstructure that differs from that of the BM. S phase precipitates (Al_2CuMg) were preferentially found at the grain and subgrain boundaries whereas the rod-shaped Al-Cu-Fe-Mn dispersoids are distributed inside the grains. Fragmentation of the rods due to friction and shear stress can take place as well as their dissolution followed by reprecipitation due to the high temperatures attained in this zone. Precipitation of coarsened S phase (Al_2CuMg) particles seems abundant in this weld zone. Bousquet *et al*. (2011) have shown that the S'(S) precipitates are gradually formed in detriment of the Al-Cu-Mn dispersoids from the HAZ region towards the TMAZ of 2024 confirming that coarsening of the S'(S) phase occurs in the TMAZ, this can be accompanied by the dissolution of smaller precipitates.

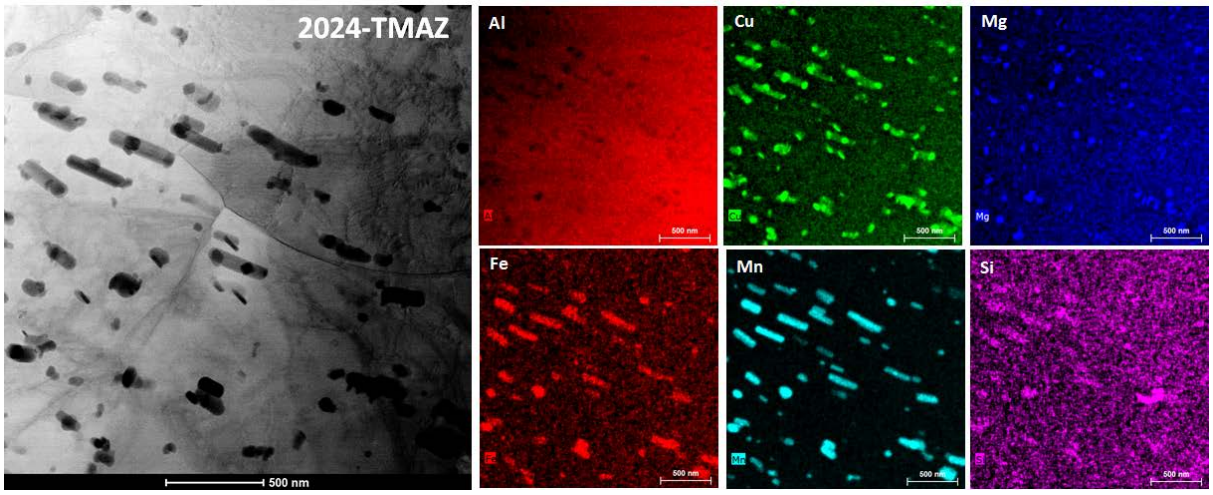

Figure 4: Micrographs obtained by Bright Field-STEM of precipitates found in the TMAZ of the 2024 alloy with EDS analysis.

Figure 5 shows micrographs obtained by TEM of the BM and the TMAZ zone of the 7475 side of the welded joint.

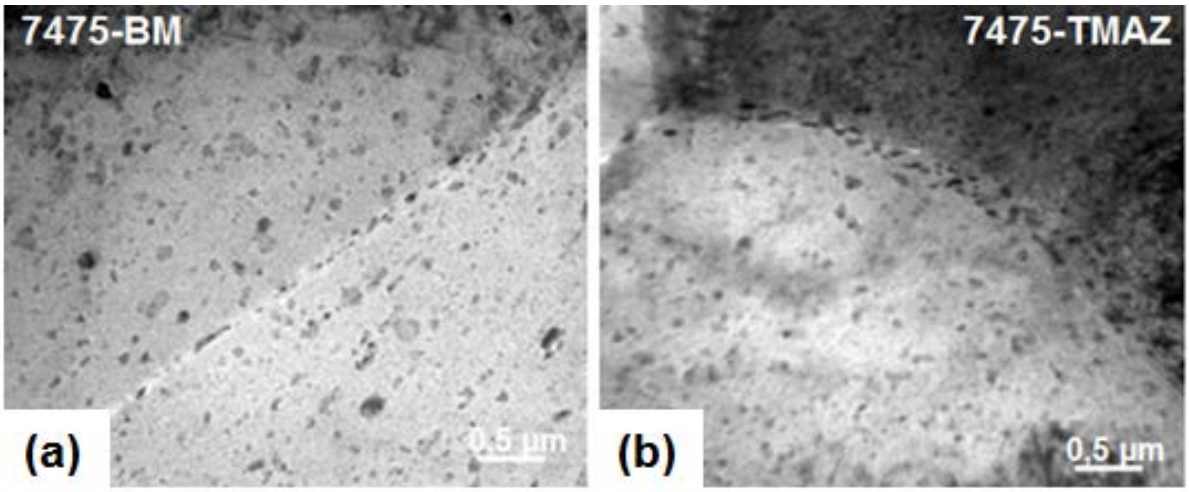

Figure 5: TEM micrographs of BM (a) and TMAZ (b) zones in the 7475 alloy joined to the 2024 by FSW.

The microstructure of the BM of the 7475 alloy (Figure 5(a)) shows fine distribution of intra-granular and intergranular precipitates ranging between 20 to 50 nm and a narrow precipitate free zone, close to the grain boundaries. Comparing to the 2024 BM this alloy seems to be more prone to intergranular precipitation. The TMAZ of the 7475 alloy shows larger amounts

of grain boundaries precipitates, suggesting that the temperatures reached in this region resulted in solubilisation followed by preferential reprecipitation. Similar results were published in the literature for FSWed 7xxx series alloys by Su *et al*. (2003) and Puydt *et al*. (2014) for 7050 and 7020 alloys, respectively. In addition, the intragranular precipitates seem to be thinner, indicating strong solubilisation. EDS analyses of precipitates in the BM and the TMAZ of 7475 alloy are shown in Figure 6.

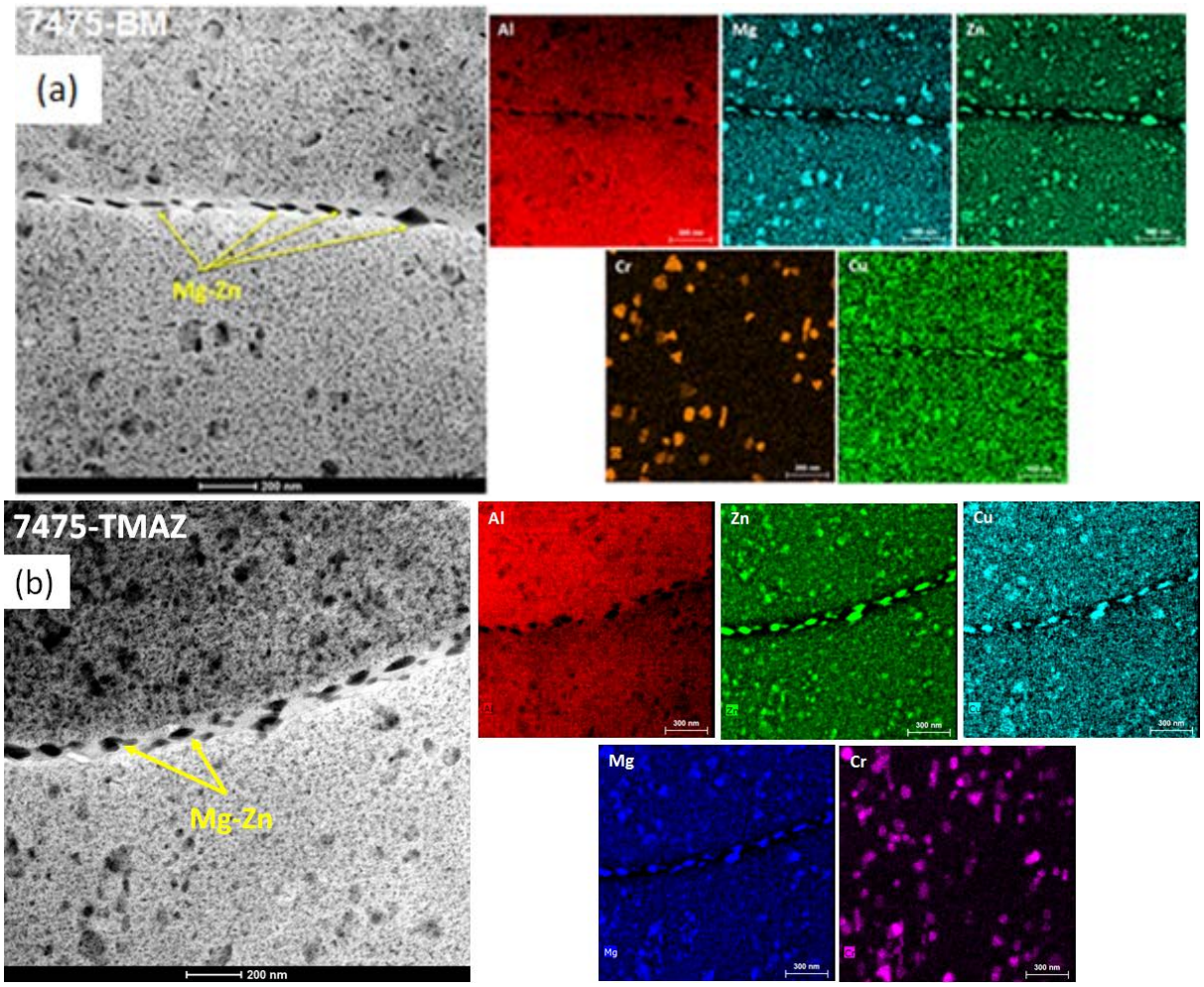

Figure 6: Bright Field-STEM micrographs of precipitates in the (a) BM and (b) TMAZ of the 7475 alloy and their EDS analyses.

According to the EDS analyses presented in Figures 6 a,b, it is observed that, independently of the region, the main precipitates found either in the BM or in the TMAZ of the 7475 alloy consist of $MgZn_2$, that is, η' and η phases. In addition, it was also found several Cr rich intragranular precipitates of geometric shapes in both regions, however, in larger amounts and smaller sizes in the TMAZ. Usually these precipitates are electrochemically inert and have no significant effect on the corrosion resistance of the alloy, apart from acting as discontinuities in the oxide film.

Figure 7 shows the DSC (Differential Scanning Calorimetry) thermograms of the BM and the TMAZ of the 2024 alloy.

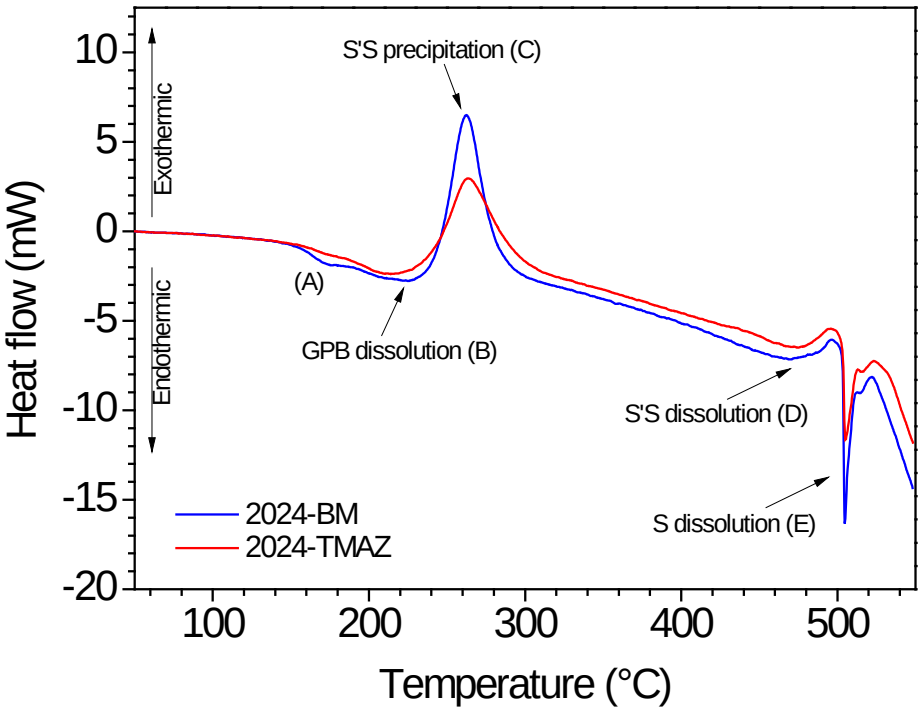

Figure 7: DSC thermograms of the BM and of the TMAZ of the 2024 alloy.

In the analysis of DSC thermograms of Figure 7, the first endothermic peak (from around 150^{o} to 250^{o}C) is ascribed to the dissolution of the GPB zones. The results indicate that smaller amount of these microstructural features are present in the TMAZ, as a lower quantity of energy was necessary to dissolve them. This is in accordance with the TEM results presented in Figures 3 and 4 as coarsening of the Al_2CuMg precipitates consumes Cu and Mg solute hindering the GPB zone nucleation during alloy storage after the FSW process. The second peak (exothermic) is related to the formation of the S '(S) phase. Accordingly, it is more intense for the 2024 BM as more solute (from the dissolution of the GPB zones) are available in this sample when compared with the S'(S) phase precipitates. As for the third and fourth (endothermic) peaks, associated with the dissolution of the S'(S) phase and S phase, respectively, they are both more intense for the BM. It is suggested that the smaller size of these precipitates in the BM make them easier to dissolve in this sample, in agreement with the literature[16].

Figure 8 shows the thermograms, obtained after DSC (Differential Scanning Calorimetry) analysis of BM and TMAZ of 7475 alloy.

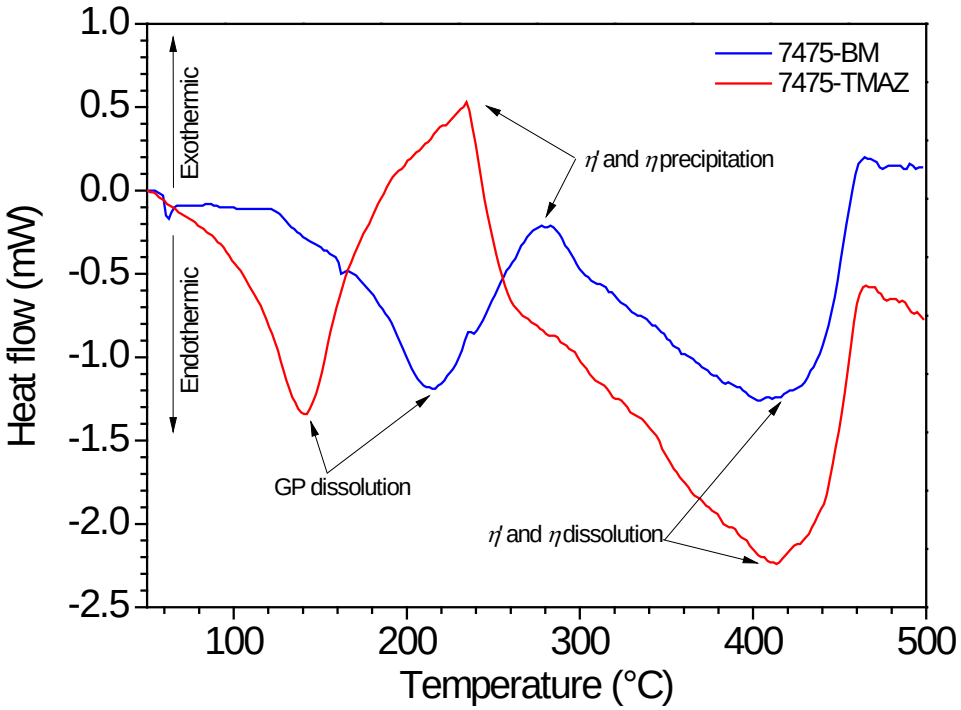

Figure 8: DSC analysis of the different zones (BM and TMAZ) of 7475 alloy, formed after the welding process by FSW.

These DSC thermograms show large differences between the responses of the two zones. The first (endothermic) peak refers to the dissolution of GP zones. It is shifted to lower temperatures for the TMAZ, indicating that the dissolution is kinetically favoured in relation to the BM. In addition, the peak is stronger, pointing to larger amount of dissolved particles. This indicates that the GP zones are more numerous and less stable in the TMAZ. The 7475 alloy is artificially aged, therefore a thermal treatment is necessary for adequate precipitation of hardening particles. Thus, it is hypothesized that the precipitation of these zone during storage of the samples after the welding procedure does not take place adequately leading to more numerous and less stable (maybe smaller) precipitates. The second peak (exothermic) is associated to η'/η phases ($MgZn_2$) precipitation. In the TMAZ it is stronger and shifted to lower temperatures, also indicating more intense precipitation and increased kinetics. This can be rationalized in terms of higher amount of solute atoms in solid solution due to increased solubility of the GP zones. The third (endothermic) peak is associated with η'/η phases ($MgZn_2$) dissolution. The higher energy required for the dissolution of these phases in the TMAZ is explained both by the previous precipitation during the DSC experiment (exothermic peak) and by the larger amounts of precipitates η'/η ($MgZn_2$) already formed in this zone during welding, mainly at the grain boundaries, in comparison to the BM. Adler and DeIasi[18] (1977), LaDelpha[19] *et al*. (2009) and Bush[20] *et al*. (2016) also observed a differences between the DSC thermograms for TMAZ and BM zones in 7xxx series alloys.

Corrosion characterization of the aluminium alloys welded by FSW

Figure 9 shows the open circuit potential (OCP) variation as a function of exposure time of the various zones of the 2024 and 7475 alloys exposed to 0.1 M Na_2SO_4 + 1 mM NaCl solution. It is important to highlight that the various zones were tested separately using a microcell (0.78 mm^2 of exposed area). However, as due to the size of the welding, for the nugget zone the two alloys are simultaneously exposed and galvanic coupling can take place. There-

fore, as expected, the OCP of the nugget zone is in-between those of the two parent metals (BM). The presence of zinc as the major alloying element in the 7475 alloy and copper in the 2024 alloy is the cause of these potentials (Hollingsworth and Hubsicker[21], 1990; Dix[22], 1998). They also indicate that in the nugget, the 2024 alloy is cathodically polarized and 7475 is anodically polarized.

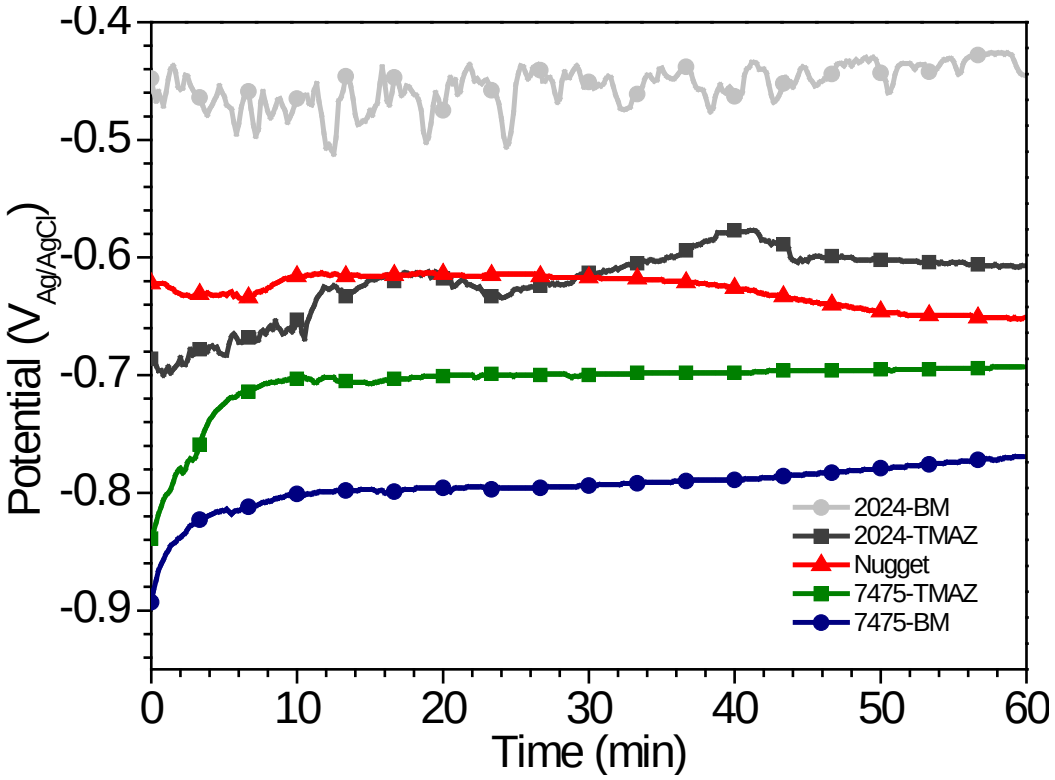

Figure 9: OCP variation with exposure time to 0.1 M Na_2SO_4 + 1 mM NaCl solution of the different zones formed during FSW of the 2024 to 7475 alloys. Data acquired using an electrochemical cell that allowed exposing a small area to the electrolyte (0.78 mm^2).

The OCP variations also show that the thermomechanical effect at the TMAZ provokes opposite responses for the 2024 and 7475 alloys. In the former the OCP is shifted to lower values whereas in the latter an increasing in the OCP was observed. This can be explained in terms of the precipitation behaviour of these alloys (Figures 4 and 6). In the 2024, the increased precipitation of Al_2Cu at the grain boundaries draws a nobler element from the alloy matrix decreasing the OCP. On the other hand, for the 7475 alloy, the precipitation of $MgZn_2$ phase withdraw more active elements from the matrix microstructure increasing the OCP. The curves of Figure 9 also indicate that after one-hour immersion the OCP is sufficiently stable to perform EIS measurements.

Anodic polarization curves of the various zones were obtained after 1.5 hour of exposure to the 0.1 M Na_2SO_4 + 1 mM NaCl solution and the results are presented in Figure 10.

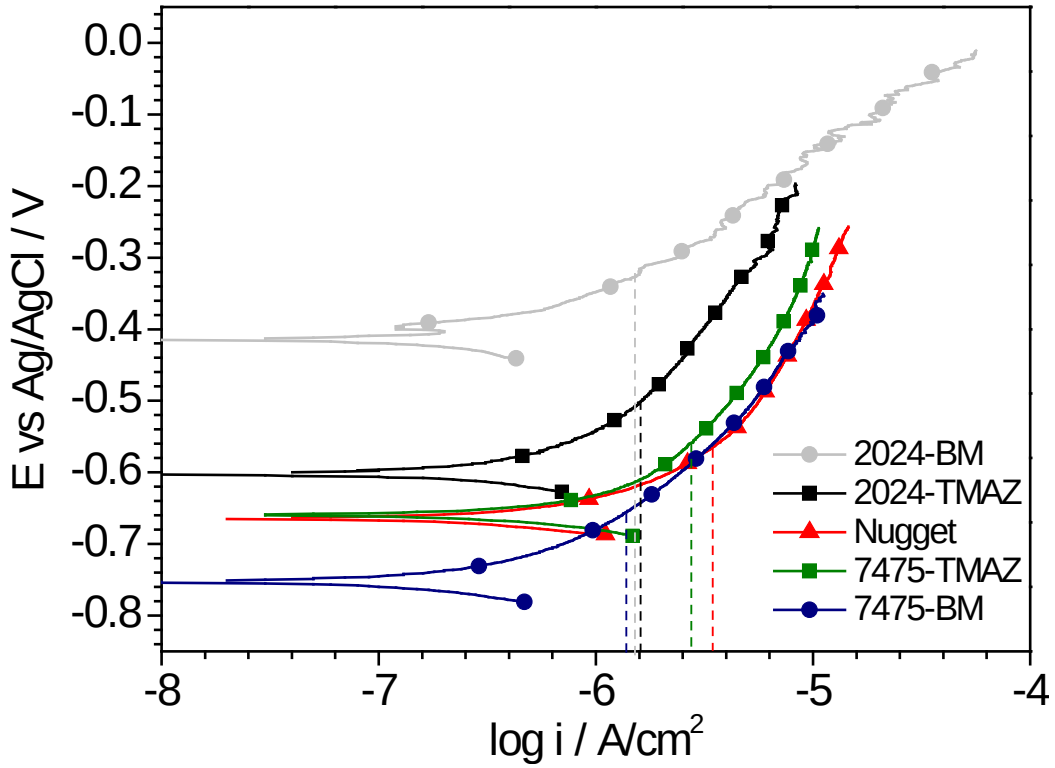

Figure 10: Anodic polarization curves in 0.1 M Na_2SO_4 + 1 mM NaCl solution of the different zones formed during FSW of the 2024 to 7475 alloys. Data acquired after 1.5 hours using an electrochemical cell that allowed exposing a small area to the electrolyte (0.78 mm^2).

Current density values were estimated for an anodic overpotential of approximately 100 mV in relation to the corrosion potential and the results are shown in Table 1. Slightly higher current densities were estimated for the nugget zone and the TMAZ of the 7475 alloy whereas very similar results were obtained for the 2024 BM, 2024 TMAZ and the 7475 BM. These results indicate the effect of galvanic coupling between the two alloys (nugget) increases the electrochemical activity in this zone. The high concentration of $MgZn_2$ precipitates in the TMAZ of the 7475 alloy, mainly located at the grain boundaries, as shown in TEM results (Figure 6 (b)) must be the reason for the increased anodic currents associated to this zone, indicating that it must be highly prone to intergranular corrosion, which is in accordance with results previously presented in the literature[23,24]. Interestingly at higher overpotential, the anodic behaviours of the nugget and of the TMAZ of the 7475 alloy are coincident, indicating the anodic behaviour of this weld zone is dominated by the response of this alloy.

Table 1: Current density values estimated at an anodic overvoltage of approximately 100 mV in relation to the corrosion potential

Region	Current density for anodic overvoltage of +100 mV / OCP
2024-BM	1.5 x10^{-6} A/cm²
2024-TMAZ	1.6 x10^{-6} A/cm²
Nugget	3.5 x10^{-6} A/cm²
7475-TMAZ	2.7 x10^{-6} A/cm²
7475-BM	1.4 x 10^{-6} A/cm²

The evolution of the EIS responses with immersion time for the different zones exposed for 1 hour to the 0.1 M Na_2SO_4 + 1 mM NaCl solution, using the microcell are shown in Figure 11.

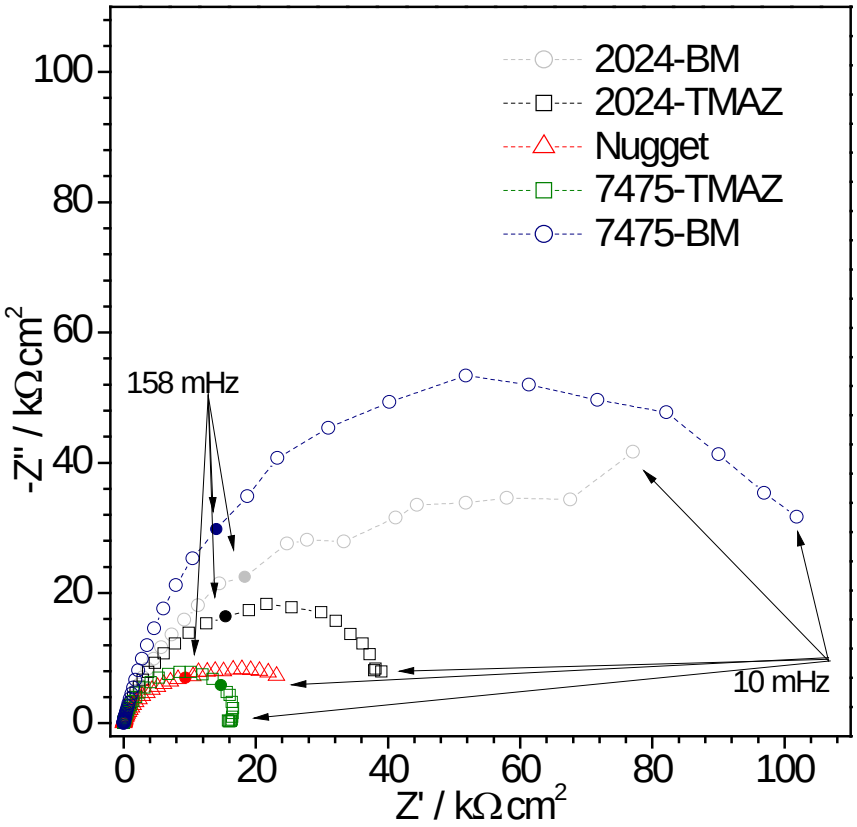

Figure 11: Nyquist diagrams in 0.1 M Na_2SO_4 + 1 mM NaCl solution of the different zones formed during FSW of the 2024 to 7475 alloys. Data acquired after 1 hour exposure using an electrochemical cell that allowed exposing a small area to the electrolyte (0.78 mm^2).

The EIS results (Figure 11) show a larger impedance for the two BM in comparison to the weld affected zones and that the BM of the 7475 presents a higher corrosion resistance when compared to the 2024. This latter finding is in accordance with previously published results and is a consequence of a more homogeneous oxide layer and lower amounts of larger intermetallic precipitates (not addressed in this study) in the microstructure of this former alloy[3,25,26]. On the other hand, the lower impedance of the welded affected zones can be explained both by microstructural changes and mechanical stresses (TMAZ – where large precipitation took place, already discussed) and to galvanic coupling effects (nugget). For both TMAZ the precipitates at the grain boundaries are anodic to their respective BM, giving rise to a higher anodic activity and a thus a lower impedance in these zones. The continuous precipitate network present at the grain boundary of the 7475 TMAZ (Figures 5 and 6) would make this zone prone to intergranular corrosion, explaining its lower impedance as well as the inductive low frequency feature (typical of localized corrosion)[27]. Besides, the low impedances of the nugget can be ascribed to galvanic coupling between the two alloys. Indeed, microstructural observation of this zone (not presented) showed increased localized attack at the 7475 alloy indicating that this alloy dominates the corrosion process.

Conclusions

The results of this work showed the effect of FSW welding on the microstructure of the TMAZ and the nugget zone and, consequently, on the corrosion resistance of these zones whose corrosion behaviour was compared with that of the two BM. The electrochemical per-

formance of each individual domain can be assessed with a specific electrochemical microcell, the size of which was adapted to the sample size. A galvanic coupling effect was observed in the nugget zone where the two aluminium alloys present a large contact surface. The TMAZ of both alloys, particularly the 7475, showed lower corrosion resistance relatively to the BM, which was related to the thermal and deformation effects on the microstructure leading to anodic intergranular precipitates increasing the susceptibility of this zone to localized attack, specifically intergranular corrosion.

Acknowledgements: Acknowledgements to CAPES (Capes/Cofecub N°.806-14) and FAPESP (Proc. 2013/13235-6) for financial support to this research.

References

[1] T. Dursun, C. Soutis, Recent developments in advanced aircraft aluminium alloys, Materials and Design 56 (2014) 962-871.
[2] C. Vargel, Corrosion of aluminium, Elsevier Amsterdam 626 (2004) 105.
[3] V. Guillaumin, G. Mankowsky, Localized corrosion of 2024-T351 aluminium alloy in chloride media, Corrosion Science 41 (1999) 421-438.
[4] W. Zhang, G.S. Frankel, Transitions between pitting and intergranular corrosion in 2024, Electrochimica Acta, 48 (2003) 1193-1210.
[5] C. Genevois, A. Deschamps, A. Denquin, B. Doisneau, Quantitative investigation of precipitation and mechanical behaviour for AA2024 friction stir welds, Acta Materialia 53 (2005) 2447-2458.
[6] J. R. Davis, Aluminium and Aluminium Alloys, ASM International Materials Park 784 (1993).
[7] J.H.W. de Witt, Local potential measurements with the SKPFM on aluminium alloys, Electrochimica Acta, 49 (2004) 2841-2850.
[8] H. J. Aval, Influences of pin profile on the mechanical and microstructural behaviors in dissimilar friction stir welded AA6082–AA7075 butt Joint, Mater. Des., 67 (2015) 413–421.
[9] D. Li, C. Mu, S. Cai, W. Lin, Ultrasonic irradiation in the enzymatic extraction of collagen, Ultrason. Sonochem., 16 (2009) 605-609.
[10] www.twi.co.uk, access 20/08/2016.
[11] M. Jariyaboon, A. Davenport, R. Ambat, B. Connolly, S. Williams, D. Price, The effect of welding parameters on the corrosion behaviour of friction stir welded, Corrosion Science, 49 (2007) 877-909.
[12] A. Bousquet, A. Poulon-Quintin, M. Puiggali, O. Devos, M. Touzet, Relationship between microstructure, microhardness and corrosion sensitivity of an 2024-T3 friction stir welded joint, Corrosion Science 53 (2011) 3026-3034.
[13] D. Sidane, E. Bousquet, O. Devos, M. Puiggali, M. Touzet, V. Vivier, A. Poulon-Quintin, Local electrochemical study of friction stir welded aluminium alloy assembly, Journal of Eletroanalytical Chemistry 737 (2015) 206-211.
[14] U. Donatus, G.E. Thompson, X. Zhou, J. Wang, A. Cassell, K. Beamish, Corrosion Susceptibility of Dissimilar Friction Stir Welds of AA5083 and AA6082 Alloys, Materials Characterization 107 (2015) 85-97.
[15] J-Q. Su, T. W. Nelson, R. Mishra, M. Mahoney, Microstructural investigation of friction stir welded 7050-T651 aluminium, Acta Materialia, 51 (2003) 713–729.

[16] Q. Puydt, S. Flouriot, S. Ringeval, F. Geuser, G. Parry, A. Deschamps, Relationship between microstructure, strenght, and fracture in an Al-Zn-Mg electron beam weld : Part I : Microstructure Characterization, Metallurgical and Materials Transactions A, 45 (2014) 6129-6140.
[17] C. Genevois, D. Fabregue, A. Deschamps, W. I. Pole, On the coupling between precipitation and plastic deformation in relation with friction stir welding of AA2024 T3 aluminium alloy, Mater. Sci. Eng. A, 441 (2006) 39–48.
[18] P.N. Adler, R. Delasi, Calorimetric studies of 7000 series aluminium alloys: II. Comparison of 7075, 7050 and RX720 alloys, Metallurgical and Materials Transactions A, 8 (1977) 1177-1183.
[19] I.A. Macaskill, A.D.P. Ladelpha, J.H. Milligan, J. Fulton, D.P. Bishop, Effects of hot and cold deformation on the mechanical performance of Alumix 431D, Powder Metall. 52 (2009) 304-310.
[20] R. Bush, M. Kiyota, C. Kiyota, Characterization of a Friction Stir Weld in Aluminum Alloy 7055 Using Microhardness, Electrical Conductivity, and Differential Scanning Calorimetry (DSC), Metallurgical and Materials Transactions A, 47 (2016) 3522-3532.
[21] E.H. Hollingsworth, H.Y. Hunsicker, Corrosion of aluminum and aluminum alloys, Handbook asm, (1990) 583.
[22] E. H. Dix, J. Rand, J. Bowman, Metals handbook asm, (1998) 804.
[23] D. A. Wadeson, Corrosion behaviour of friction stir welding AA7108-T79 aluminium alloy, Corrosion Science, 48 (2006) 887-897.
[24] J. Lumsdem, M. Mahoney, C. Rhodes, G. Pollock, Corrosion Behavior of Friction-Stir-Welded AA7050-T7651, Corrosion Science, 59 (2003) 212-219.
[25] R. G. Buccheit, R. P. Grant, P. F. Hlava, B. Mckenzie, G. L. Zender, Local Dissolution Phenomena Associated with S Phase (Al_2CuMg) Particles in Aluminium Alloy 2024-T3, Journal of the Electrochemical Society, 144 (1997) 2621.
[26] J. Wloka, S. Virtanen, Microstructural Effects on the Corrosion Behavior of High-Stenght Al-Zn-Mg-Cu Alloys in an Overaged Condition, Journal of the Electrochemical Society, 154 (2007) 411-C423.
[27] F. Mansfeld, J. C. S. Fernandes, Impedance spectra for aluminum 7075 during the early stages of immersion in sodium chloride, Corrosion Science, 34 (1993) 2105-2108.